

Rapid, Micron-Resolution 3D Printing of Nd:YAG Ceramic with Optical Gain

Luyang Liu, Wenbo Wang, Shuai Feng, Siying Liu, Haofan Sun, Qiong Nian, Sui Yang, and Xiangfan Chen*

Polycrystalline yttrium aluminum garnet (YAG) ceramic doped with neodymium (Nd), referred to as Nd:YAG, is widely used in solid-state lasers. However, conventional powder metallurgy methods suffer from expenses, time consumption, and limitations in customizing structures. This study introduces a novel approach for creating Nd:YAG ceramics with 3D free-form structures from micron (~70 µm) to centimeter scales. Firstly, sol-gel synthesis is employed to form photocurable colloidal solutions. Subsequently, by utilizing a home-built micro-continuous liquid interface printing process, precursors are printed into 3D poly(acrylic acid) hydrogels containing yttrium, aluminum, and neodymium hydroxides, with a resolution of 5.8 μ m pixel⁻¹ at a speed of 10 μ m s⁻¹. After the hydrogels undergo thermal dehydration, debinding, and sintering, polycrystalline Nd:YAG ceramics featuring distinguishable grains are successfully produced. By optimizing the concentrations of the sintering aids (tetraethyl orthosilicate) and neodymium trichloride (NdCl₃), the resultant samples exhibit satisfactory photoluminescence, emitting light concentrated at 1064 nm when stimulated by a 532 nm laser. Additionally, Nd:YAG ceramics with various 3D geometries (e.g., cone, spiral, and angled pillar) are printed and characterized, which demonstrates the potential for applications, such as laser and amplifier fibers, couplers, and splitters in optical circuits, as well as gain metamaterials or metasurfaces.

1. Introduction

Solid-state lasers have gained considerable attention across scientific and industrial domains for their ability to generate coherent radiation, high-quality beams, tunable wavelengths, compactness, and durability.^[1–3] The gain media frequently employed

L. Liu, W. Wang, S. Liu, X. Chen
School of Manufacturing Systems and Networks
Arizona State University
Mesa, AZ 85212, USA
E-mail: Xiangfan.Chen@asu.edu
S. Feng, S. Liu, H. Sun, Q. Nian, S. Yang
School for Engineering of Matter
Transport & Energy
Arizona State University
Tempe, AZ 85287, USA

The ORCID identification number(s) for the author(s) of this article can be found under https://doi.org/10.1002/smll.202403130

DOI: 10.1002/smll.202403130

in solid-state lasers are crystalline ceramics doped with rare-earth metal elements, such as neodymium-doped yttrium orthovanadate and titanium-doped sapphire.[4-7] Particularly, polycrystalline yttrium aluminum garnet (Y₃Al₅O₁₂, i.e., YAG) ceramic doped with neodymium (Nd), known as Nd:YAG, has emerged as a prominent choice for solid-state lasers utilized in medical treatments, [8-16] manufacturing industries,[17-19] and characterization tools (e.g., cavity ring-down spectroscopy).[20] This is primarily attributed to its exceptional properties, such as efficient wavelength, high energy density, versatility, and reliability.[3,21] Particularly, specific applications demand customized 3D geometries of lasing media to meet unique operational needs, such as optical fiber couplers and splitters in optical circuits,[21] as well as multi-point laser ignitors for engines.[22]

Conventionally, the fabrication of Nd:YAG structures mainly relies on powder metallurgy methods. [23–26] In those approaches, powders, including yttrium oxide (Y₂O₃), aluminum oxide (Al₂O₃), neodymium oxide (Nd₂O₃), and silicon oxide (SiO₂), are mechanically mixed and

compacted within molds, followed by sintering under vacuum conditions at elevated temperatures. [27] However, those methods usually come with several inherent limitations. For instance, creating molds with high rigidity and customized 3D structures featuring micron-scale (um-scale) details is both time-consuming and cost-prohibitive. Besides, compaction pressure cannot be delivered to all the geometrical features efficiently, and the flow of powder into these micron-scale features is hindered by the large friction force. Consequently, attaining uniform powder dispersion within the mold typically requires a prolonged mechanical stirring or compaction, usually exceeding 24 hours, and in certain intricate molds, achieving homogeneous distribution is essentially unattainable.^[26] These limitations impose significant constraints on feasible product dimensions and structural complexity. Moreover, the machinery necessary for vacuum sintering at high temperatures is costly and energy-intensive.

Alternatively, additive manufacturing (AM), also known as 3D printing, has emerged as a promising method for creating 3D free-form ceramics to address specific needs.^[28–35] In particular, approaches such as direct ink writing (DIW),

www.small-journal.com

16136582, 2024, 36, Downloaded from https://onlinelibrary.wikey.com/doi/10.1002/sml1.202403130 by Arizon State University Acq. Wiley Online Library on [17/102024]. See the Terms and Conditions (https://onlinelibrary.wikey.com/ems-and-conditions) on Wiley Online Library or rules of use; OA articles are governed by the applicable Centitive Commons the Terms and Conditions (https://onlinelibrary.wikey.com/ems-and-conditions) on Wiley Online Library for rules of use; OA articles are governed by the applicable Centitive Commons the Terms and Conditions (https://onlinelibrary.wikey.com/ems-and-conditions) on Wiley Online Library for rules of use; OA articles are governed by the applicable Centitive Commons that the terms and Conditions (https://onlinelibrary.wikey.com/ems-and-conditions) on Wiley Online Library for rules of use; OA articles are governed by the applicable Centitive Commons that the terms and Conditions (https://onlinelibrary.wikey.com/ems-and-conditions) on Wiley Online Library for rules of use; OA articles are governed by the applicable Centitive Commons that the terms and Conditions (https://onlinelibrary.wikey.com/ems-and-conditions) on Wiley Online Library for rules of use; OA articles are governed by the applicable Centitive Commons that the terms and Conditions (https://onlinelibrary.wikey.com/ems-and-conditions) on Wiley Online Library for rules of use; OA articles are governed by the applicable Centitive Commons that the terms and conditions (https://onlinelibrary.wikey.com/ems-and-conditions) on Wiley Online Library for rules of use; OA articles are governed by the applicable Centitive Commons that the terms and conditions (https://onlinelibrary.wikey.com/ems-and-conditions) on Wiley Online Library for rules of use; OA articles are governed by the applicable Centitive Commons that the terms and conditions (https://onlinelibrary.wikey.com/ems-and-conditions) on Wiley Online Library for rules of use; OA articles are governed by the applicable Centitive Commons that the terms and conditions (htt

stereolithography (SLA), and digital light processing (DLP), have been reported to fabricate polycrystalline YAG ceramics with tailored optical properties. [28,34,35,36] For example, Zhang et al. used DIW to print a composite ink comprising Y₂O₃ and Al₂O₃ powders, a polymer plasticizer, and a binder. [30] The as-printed samples were then sintered, during which polycrystalline YAG was synthesized through the solid-state reaction between Al₂O₃ and Y₂O₃ at elevated temperatures (1750 °C) in a vacuum environment. However, only simple 3D shapes (e.g., gears and core-shell rods) were printed by using DIW, [30,37] and the printing speed is limited due to the point-by-point scanning nature. On the other hand, Zhang et al. also successfully printed 3D composites containing Nd₂O₃, Y₂O₃, and Al₂O₃ powders by DLP.^[38] The printed polymer-ceramic composites were then sintered to achieve polycrystalline Nd:YAG. [38] Nonetheless, all those aforementioned 3D printing methods still suffer from drawbacks associated with the nanoparticle-dispersed resins. For instance, particle agglomeration and precipitation tend to occur during printing and become more pronounced in the slow DIW and DLP processes, [39] resulting in the composition inhomogeneity of the printed samples. The inhomogeneity not only hampers shape retention during post-sintering, but also compromises the mechanical and optical properties of the final products.[40-44]

Recently, instead of synthesizing YAG through solid-state reaction from dispersed solid particles, sol-gel synthesis starting with liquid solutions has been integrated into photopolymerizationbased 3D printing to produce Nd:YAG. The sol-gel synthesis typically involves the following steps: 1) dissolving metal chlorides or metal alkoxides in solvents and mixing them with photocurable monomers, 2) initiating hydrolysis to form hydroxide groups and colloidal solutions (sol), and 3) condensing and gelation of sols during the photopolymerization of monomers, resulting in the formation of a 3D network of hydrogels. [45] Utilizing an entire liquid-phase precursor system in sol-gel synthesis, which exhibits decreased viscosity and advantageous optical characteristics compared to slurries, leads to a significant enhancement in printability and a notable reduction in fabrication time. [46] More importantly, the stable and homogeneous precursor ensures composition homogeneity in the product and potentially facilitates lower processing temperatures.^[45] For example, Cooperstein et al. reported using two-photon photopolymerization (TPP) laser writing with sol-gel synthesis and post-sintering to fabricate um-size polycrystalline Nd:YAG structures.[45] On the other hand, TPP has been demonstrated to successfully fabricate various optical elements with optical gain. For instance, Gao et al. employed TPP to produce µm-scale erbium-doped polymeric waveguide amplifiers. [47] While TPP provides remarkable sub-um resolution and the capability to photopolymerize at specific points within the liquid resin, its printing speed is notably slow, and the build volume is typically limited to tens to hundreds of µm.[48] This limitation renders it unsuitable for certain applications requiring large-scale Nd:YAG structures, such as millimeter-scale optical fiber couplers for hysteroscopy procedures.^[49]

Herein, as shown in Figure 1, we present a novel 3D printing approach to fabricate multi-scale polycrystalline Nd:YAG ceramics with customized 3D structures. This method involves two stages: (1) integrating sol-gel synthesis with 3D printing to print photocurable resins comprising dissolved metal chlorides into hydrogels containing metal hydroxides using a home-built micro-continuous liquid interface printing (μCLIP) process; [39,50] and (2) thermal debinding and sintering the printed hydrogels, leading to the pyrolysis of the polymer matrix and the formation of polycrystalline Nd:YAG ceramics. By precisely adjusting concentrations for sintering aids and Nd doping, we achieved tunable and satisfactory photoluminescence (PL) in Nd-doped samples, which can emit 1064 nm light upon 532 nm laser excitation. Furthermore, we successfully prototyped and tested Nd:YAG ceramics with various 3D geometries, with which we could visualize the emitted light (1064 nm) from the output ends when irradiated at the input ends of sintered parts, thus confirming their potential as lasing media.

2. Results and Discussion

In the initial stage, as depicted in Figure 1a, upon dissolution in the solvent, the hydrolysis of yttrium chlorides (YCl₃), aluminum chlorides (AlCl₃), and neodymium chlorides (NdCl₃) leads to the formation of yttrium hydroxide (Y(OH)₃), aluminum hydroxide (Al(OH)₃), neodymium hydroxide (Nd(OH)₃), protons, and chlorine ions, which resulted in a decrease in the system's pH. Propylene oxide (PO) serves as an accelerator by scavenging protons and chlorine ions, thereby raising the pH and expediting the condensation of hydroxides to form a colloidal solution (sol). [48,51] Acrylic acid (AAc) is chosen as the monomer, along with a photoinitiator and a UV absorber, to enable photopolymerization. Subsequently, as shown in Figure 1b, the μ CLIP is used to print 3D free-form structures. This system incorporates a transparent, oxygen-permeable resin bath window, creating a polymerizationfree "dead zone". [52-55] This "dead zone" enables continuous resin replenishment and significantly increases the printing speed, [54] thus overcoming the slow printing speeds associated with other DLP or TPP processes. To achieve desirable geometry accuracy, optimal printing parameters are determined by using a speedworking curve model (Figure S1, Supporting Information).[39,56] Specifically, the optimal printing speed for the aforementioned photocurable resin is 10 $\mu m\ s^{-1}$, with an illuminating light intensity of 8 mW cm⁻², allowing for precise printing of sophisticated 3D structures, such as the Kelvin cell lattice with a layer slicing thickness of 5 µm (CAD model and geometry parameters are provided in Figure S2a and Table S1, Supporting Information). As shown in Figure 1c, the resultant hydrogel is a poly(acrylic acid) PAAc-based network infused with interstitial fluid comprising the solvent, metal hydroxides, and a sintering aid. [57–59] From a compositional perspective, the Raman spectrum of the freezedried hydrogel confirms the occurrence of the sol-gel reaction, which is based on the identification of characteristic peaks corresponding to chemical bonds (i.e., Y-OH, Nd-OH, and Al-O-Al) within metal hydroxides (Figure S3 and Table S2, Supporting Information). In the subsequent phase, the as-printed hydrogels undergo dehydration and pyrolysis at 620 °C, followed by sintering at 1650 °C under atmospheric air (Experimental Section). This process leads to the formation of the polycrystalline Nd:YAG structure, [45] as shown in Figure 1d. The scanning electron microscopy (SEM) image in Figure 1e reveals the grains within the sintered Kelvin cell lattice, showcasing distinct grain boundaries as evidence of successful crystallization during the sintering process. After sintering, the fabricated samples can emit light at a

16136829,2024, 36, Downloaded from https://onlinelibrary.wiley.com/doi/10.1002/smll 202403130 by Arizona State University Acq, Wiley Online Library on [17/10/2024]. See the Terms and Conditions (https://onlinelibrary.wiley.com/term

ss) on Wiley Online Library for rules of use; OA articles are governed by the applicable Creative Commons

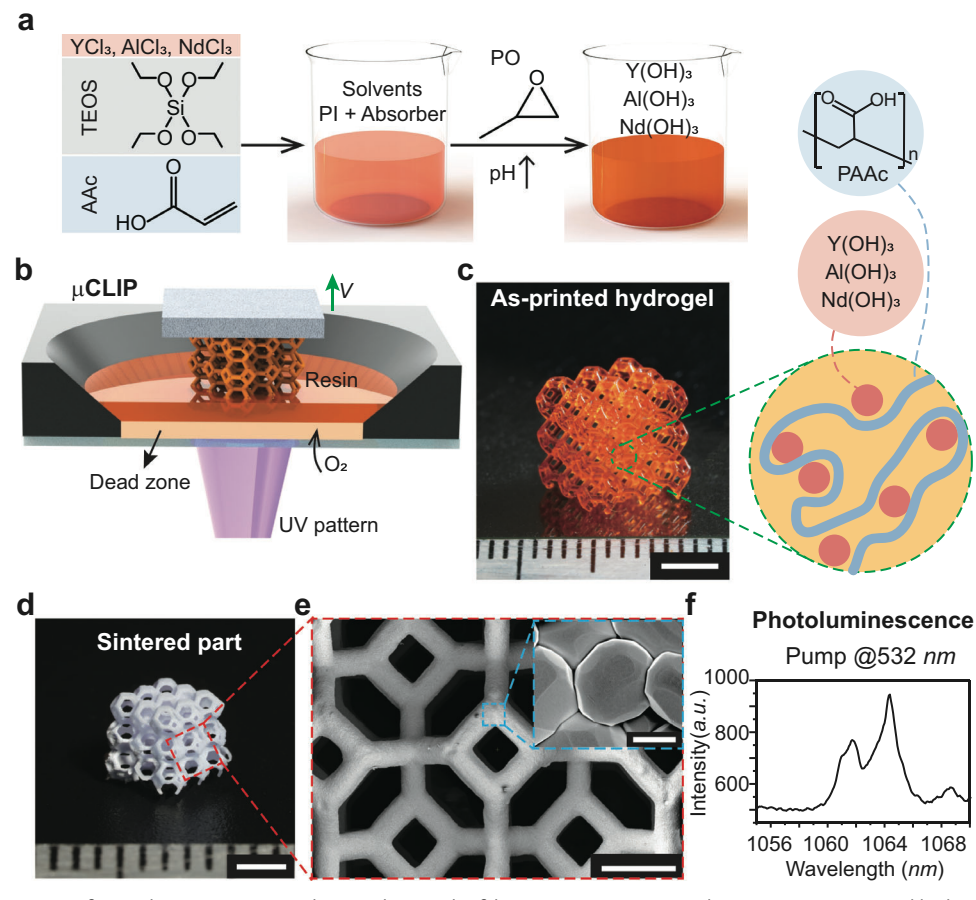


Figure 1. Fabrication steps of 3D Nd:YAG ceramics with optical gain. The fabrication processes involve (a) generating metal hydroxide "sol" from metal chloride solutions; (b) utilizing the µCLIP to rapidly print the "sol" into PAAc-based hydrogel structures (c); and (d) producing polycrystalline Nd:YAG ceramics through sintering. (e) SEM image of the sintered sample. (f) A representative PL spectrum of the sintered sample. Scale bars: 4 mm (c), 2 mm (d), 400 μ m (e), 2 μ m (inset in e).

wavelength of 1064 nm when excited by a 532 nm laser, as depicted in the PL spectrum in Figure 1f.

In the PL process, Nd ions within the Nd:YAG crystal can absorb photons from the pump laser, raising their energy levels to the excited state.^[1] Upon returning to a lower energy state, these excited Nd ions release energy in the form of photons, resulting in light emission at the specific wavelength of 1064 nm.^[60] However, in polycrystalline ceramics, factors such as grain boundaries or pores can cause significant scattering,[61,62] negatively affecting the PL performance. Therefore, achieving the production of polycrystalline Nd:YAG ceramics with outstanding uniformity and minimal porosity is crucial for ensuring satisfactory PL performance. To accomplish this goal, we introduced tetraethyl orthosilicate (TEOS) as a sintering aid in our photocurable resin. The TEOS can undergo pyrolysis and decompose into SiO₂, which subsequently reacts with YAG at 1380 °C and forms a liquid phase during sintering.^[63] This liquid phase can facilitate particle rearrangement and mass transportation through grain-boundary diffusion, ultimately leading to improved ceramic properties and reduced porosity. [64]

To achieve ideal PL performance, a comprehensive study was conducted to determine the optimal concentration of TEOS and NdCl₃. In detail, a series of representative samples, i.e., queen chess pieces, were printed from resins with TEOS concentrations ranging from 0 wt% to 2 wt%, as shown in Figure S4a-S4e, Supporting Information. The concentration of NdCl₃ was selected to be 0.6 wt% according to the literature. [45] Detailed compositions of the resins are listed in Table \$3, Supporting Information. The as-printed hydrogels then underwent an identical sintering process (Experimental Section). Optical and SEM images of the sintered parts are shown in Figure 2a-e. In the absence of TEOS, as depicted in the SEM images, the majority of the grain sizes are generally small (a_2-a_5) with an average grain size of $1.91 \pm 1.79 \,\mu m$ (Figure 2f). More importantly, abnormal grain growth was observed, as indicated by some large grains sporadically dispersed within the microstructure (Figure 2a₄ & 2a₅), ^[63] as well as the outliers in the box plot of the grain sizes (Figure 2f) (characterization of these outliers is described in Section 6, Supporting Information). Correspondingly, the calculated porosity was relatively high (16.71 \pm 4.45%) (Figure 2g) (calculation in Figure S5, Supporting Information). As mentioned above, this is attributed to reduced intergranular diffusion coefficients and increased surface energy of the grains. [64] This also results in limited macroscopic shape retention of the sintered parts (a_1) . The abnormal grain growth disappears when increasing the TEOS concentration from 0.5 wt% to 1 wt%, because of the increased

16136829, 2024, 36, Downloaded from https://onlinelibrary.wiley.com/doi/10.1002/smll.202403130 by Arizona State University Acq, Wiley Online Library on [17/10/2024]. See the Terms and Conditions (https://onlinelibrary.wiley.com/doi/10.1002/smll.202403130 by Arizona State University Acq, Wiley Online Library on [17/10/2024]. See the Terms and Conditions (https://onlinelibrary.wiley.com/doi/10.1002/smll.202403130 by Arizona State University Acq, Wiley Online Library on [17/10/2024]. See the Terms and Conditions (https://onlinelibrary.wiley.com/doi/10.1002/smll.202403130 by Arizona State University Acq, Wiley Online Library on [17/10/2024]. See the Terms and Conditions (https://onlinelibrary.wiley.com/doi/10.1002/smll.202403130 by Arizona State University Acq, Wiley Online Library on [17/10/2024]. See the Terms and Conditions (https://onlinelibrary.wiley.com/doi/10.1002/smll.202403130 by Arizona State University Acq, Wiley Online Library on [17/10/2024].

on Wiley Online Library for rules of use; OA articles are governed by the applicable Creative Comm

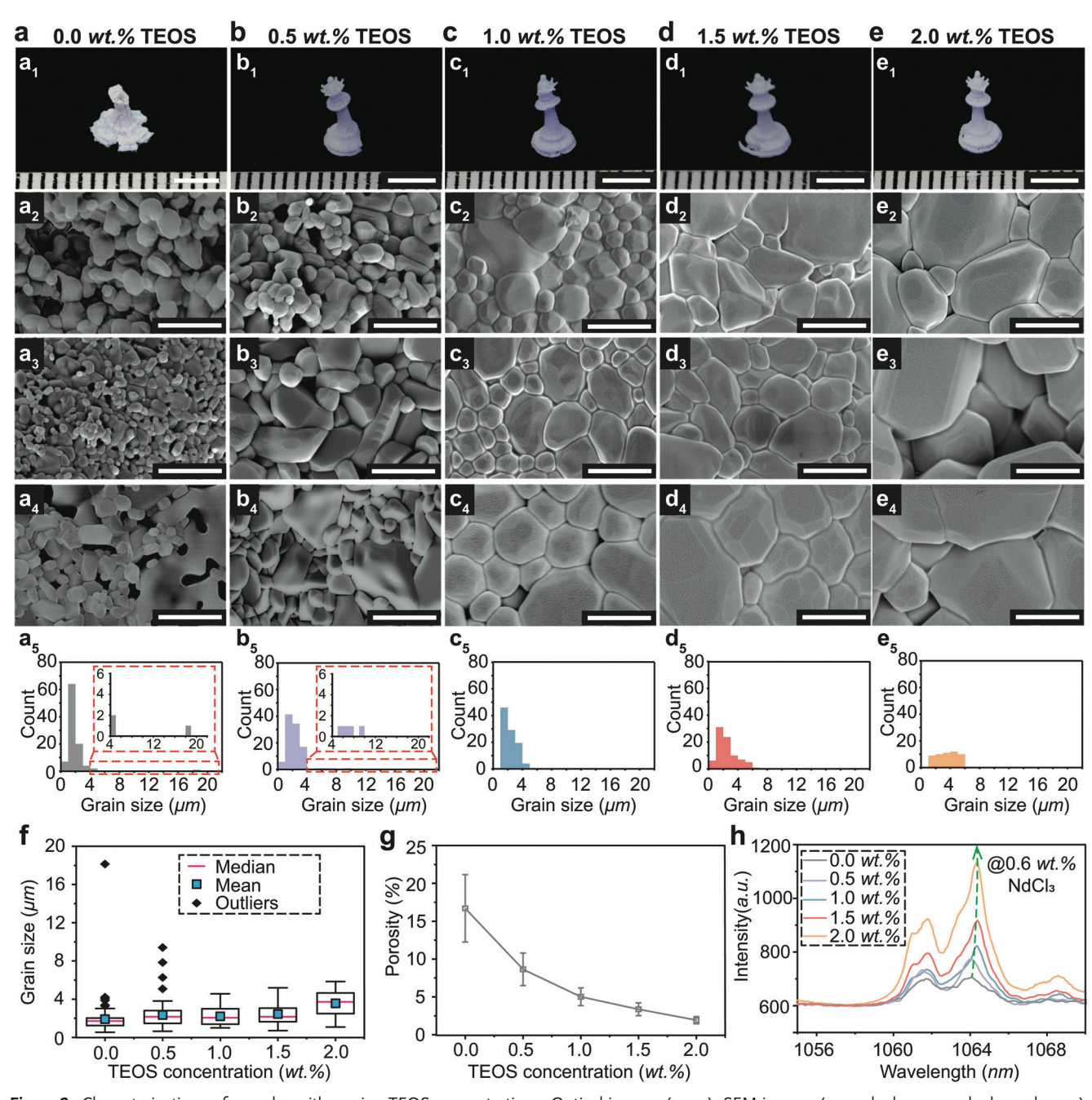


Figure 2. Characterizations of samples with varying TEOS concentrations. Optical images (a1-e1), SEM images (a2-a4, b2-b4, c2-c4, d2-d4, and e2-e4), and corresponding grain size distribution (a_s-e_s) of sintered queen chess pieces with varying TEOS concentrations. (f) Box plot of grain sizes and corresponding porosities (g). (h) PL spectra of thin plate samples with different TEOS concentrations. Scale bars: 4 mm (a₁-e₁), 4 µm (a₂-e₄).

grain boundary diffusion rate, as shown in Figure 2f.[64] By further increasing the TEOS concentration up to 2 wt%, samples with a more uniform and larger grain size, as well as reduced porosity, are obtained (Figure 2b-2e). In detail, the average grain size expanded to 3.57 \pm 1.37 μm , and the porosity decreased to 1.93 \pm 0.48%. These improvements in microstructures collectively resulted in a denser structure with satisfactory shape retention after sintering, as depicted in Figure 2e1. Additionally, energy-dispersive X-ray spectroscopy (EDS) measurements

(Table \$4, Supporting Information) confirmed that the atomic ratio of Yttrium (Y), Aluminum (Al), and Oxygen(O) within the sintered parts remained consistent at approximately 3:5:12, aligning with samples fabricated through conventional powder metallurgy methods.[25]

Then, PL spectra were measured by using a confocal Raman microscope (Alpha300 RA Ramen-AFM Microscope, WITec). Standard thin plate samples were printed, sintered (Figure S6a and Table S5, Supporting Information), and excited by a 532 nm

16136829, 2024, 36, Downloaded from https:

://onlinelibrary.wiley.com/doi/10.1002/smll.202403130 by Arizona State University Acq, Wiley Online Library on [17/10/2024]. See the Terms

conditions) on Wiley Online Library for rules of use; OA articles are governed by the applicable Creative Commons

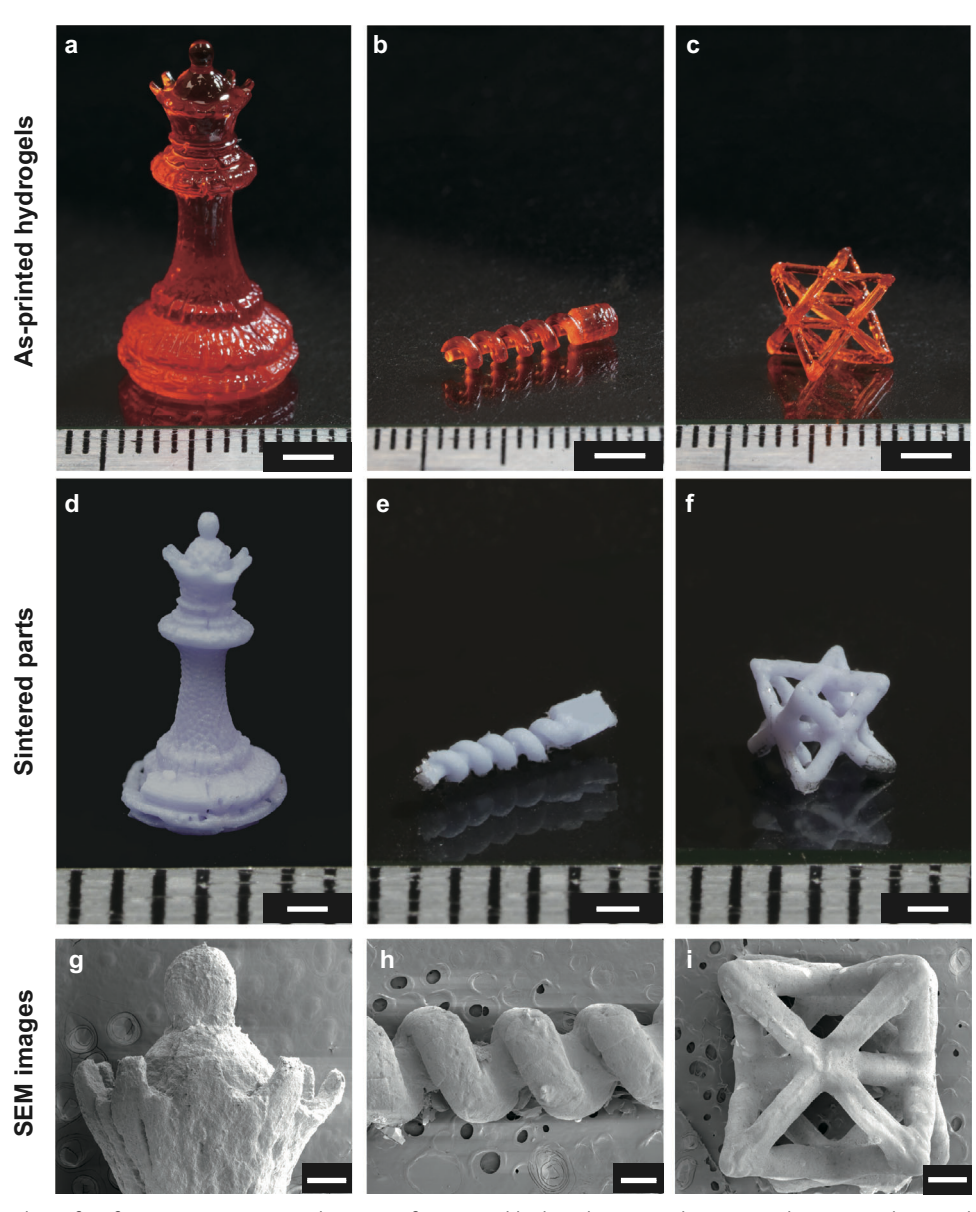


Figure 3. Samples with 3D free-form structures. Optical images of as-printed hydrogels (a-c) and corresponding sintered parts (d-f) featuring a queen chess piece (a, d), a spiral (b, e), and an octet truss cell (c, f). SEM images of sintered parts, including a queen chess piece (g), a spiral (h), and an octet truss cell (i). Scale bars: 3 mm (a-c), 1 mm (d-f), and 400 µm (g-i).

laser with an intensity of ~10 mW cm⁻² (Figure S7, Supporting Information). Figure 2g presents PL spectra ranging from 1055 nm to 1070 nm for samples printed from resins with TEOS concentrations of 0 wt%- 2 wt%. Remarkably, the peak intensity of PL around 1064 nm increases monotonously with the rise of TEOS concentration. These findings demonstrate that elevating the concentration of TEOS in the precursor benefits a denser structure with improved grain arrangement and reduced porosity, diminishing the scattering caused by pores or grain boundaries. Given these outcomes, a TEOS concentration of 2 wt% was chosen for all subsequent experiments. Subsequently, we employed the optimal TEOS concentration to 3D print hydrogels with diverse structures, showcasing the versatility of our approach. As illustrated in the optical images in Figure 3a-c, these structures include a queen chess piece, a spiral, and an octet truss cell (geometry parameters are provided in Figure S2 and Table S1, Supporting Information). Optical images of the corresponding sintered parts in Figure 3d-f and SEM images in Figure 3g-i demonstrate the satisfactory preservation of intricate features, such as the crown of the queen chess piece and the micro-scale beams in the octet truss cell. Despite the significant volume shrinkage (~87.5%) after sintering, the height of the queen chess piece still measures approximately 1 cm, and the smallest beam diameter in the Kelvin cell lattice (Figure 1d) is around 70 μm. These results affirm our approach's capability to fabricate freeform and multi-scale structures spanning from micron to centimeter scales.

1613689, 2024, 36, Downloaded from http://onlinelibrary.wiky.com/doi/10.1002/sml1.202403130 by Arizona Sate University Acq. Wiley Online Library on [171102024]. See the Terms and Conditions (https://onlinelibrary.wiky.com/rems-and-conditions) on Wiley Online Library or rules of use; OA articles are governed by the applicable Creative Commons the Commons of the Common of the Com

To enhance PL performance, in addition to considering printability, it's crucial to make an optimal choice regarding the concentration of Nd doping. This is because a higher concentration of Nd ions within YAG ceramics will provide numerous sites that can efficiently absorb incident photons and get excited, resulting in a proportional increase in the overall emitted intensity.[65] To optimize the Nd concentration, a series of standard thin plates (Figure S6 and Table S5, Supporting Information) were printed from resins with NdCl₃ concentration ranging from 0 wt% to 2.4 wt%. Resin compositions are detailed in Table S6, Supporting Information. EDS analysis indicated that, aside from Nd, the atomic ratios of other elements (i.e., Y, Al, and O) remained nearly constant at 3: 5: 12 (Figure 4a). EDS mappings (Figure 4b) confirmed the uniform dispersion of the elements (i.e., Y, Al, and Nd) within the sintered parts. SEM images revealed that different concentrations of Nd element only resulted in minor alterations in the microstructure. The average grain size and porosity are approximately 3.66 \pm 1.13 μm and 2.06 \pm 0.35%, respectively (Figures 4c and S8, Supporting Information). Subsequently, as shown in Figure 4d, the PL performance of these samples was characterized using the same method employed for sintering aid optimization (Figure \$7, Supporting Information). It was found that the peak PL intensity around 1064 nm increased monotonously with the elevation of Nd concentration while maintaining a constant pump laser intensity of $\sim 10 \text{ mW cm}^{-2}$.

Additionally, since excitation light intensity also affects PL emission intensity, PL spectra were measured for samples with varying Nd doping when excited by a 532 nm laser with varying intensities to assess the PL performance comprehensively. [66] Figure 4e presents the measured peak intensities of PL around 1064 nm. These peak intensities monotonously increase with the rise in Nd concentration at most pump laser intensities, except at 1 mW cm⁻². This discrepancy can be attributed to concentration quenching observed for low excitation rates at lower pump laser intensities.^[67] During the PL process, when Nd ions transition back to their lower energy state, not all excited electrons within Nd ions return to their ground state. Some electrons become trapped by positively charged intrinsic defects. [68,69] At higher pump laser intensities, these entrapped electrons can be re-excited, allowing all excited electrons to revert to the ground state, releasing the absorbed energy in the form of photons. Conversely, at lower pump laser intensity (i.e., 1 mW cm⁻²), electrons ensnared within intrinsic defects remain unresponsive to re-excitation, resulting in a partial release of absorbed energy. Collectively, these results highlight that increased Nd doping provides more active sites for absorbing photons, leading to improved PL performance when the pump laser intensity is raised. Based on these findings, an NdCl₃ concentration of 2.4 wt% was chosen for all subsequent characterizations.

After carefully optimizing the TEOS and Nd concentrations, we successfully produced polycrystalline Nd:YAG ceramic with favorable PL performance under excitation at a pump intensity of 50 mW cm⁻² (Figure 4e). To visualize the emitted light centered around 1064 nm, as illustrated in Figure S9, Supporting Information, we conducted PL imaging measurements using a modified inverted microscope (Axio Observer D1m, Zeiss). Various structures, including a cone (**Figure 5** a_1), a spiral (Figure 5 a_2), and angled pillars (Figure 5a₃ & 5a₄), were printed, sintered, and observed using the inverted microscope equipped with a halogen light source (QTH10, Thorlabs), as shown in Figure $5b_1-5b_4$. The resin compositions are detailed in Table \$7. Supporting Information. Subsequently, samples' input ends were irradiated by a 532 nm laser at a 45° incident angle with respect to the horizontal plane, and the images of emission were collected at the samples' output ends, as illustrated in Figures 5c₁-5c₄ and S9, Supporting Information. A long-pass filter with a cut-on wavelength of 594 nm was employed to eliminate light with shorter wavelength (i.e., pump laser). The images of the excited samples were captured and shown in Figure $5d_1-5d_4$, in which the bright samples undeniably affirm the presence of discernible emitted PL signals from the output ends. These findings provide visual evidence of the potential applicability of the printed Nd:YAG samples as optical components with gain, such as optical fibers, couplers, and splitters.

In Nd: YAG-based lasing media, achieving high transparency is paramount. Nd: YAG ceramics with high transparency ensure efficient absorption of optical energy from the pumping sources. This absorption is essential for creating the population inversion required for stimulated emission and subsequent laser output. However, it is worth mentioning that when compared to the samples produced by conventional methods, [25] there is still room for enhancing the transmittance of the printed parts. The maximum transmission of samples with a thickness of ~7 µm is 56.79% within the visible wavelength range (Figure \$10,\$11, Supporting Information). This reduction in transmittance can be attributed to the polycrystalline grain size observed in our samples, ranging from 1 µm to 4 µm (Figure 2f), causing significant light scattering at grain boundaries. Previous studies have also indicated that in polycrystalline YAG ceramics, transmittance significantly decreases in samples with an average grain size within the range of 1 µm to 4 µm compared to those with grain sizes exceeding 8 μm.^[70] To improve transparency, our future efforts will focus on improving grain arrangement by employing special sintering processes, such as spark plasma sintering. [62] Subsequently, the influence of the TEOS and Nd concentration on the transparency will also be subjected to further investigation.

3. Conclusion

In summary, this study has successfully demonstrated the rapid 3D printing of customized polycrystalline Nd:YAG ceramics. The high-speed and high-resolution 3D printing technique, μCLIP, effectively addresses limitations inherent in other additive manufacturing methods previously reported to successfully fabricate ceramics with optical gain.^[71] These limitations include the trade-off between speed and accuracy associated with DIW and the constrained printing area of TPP.[47] Besides, this solgel reaction-based method ensures uniformity and consistency in the composition of the as-printed structures compared to previous slurry-based 3D printing methods.[30,38] The sintered Nd:YAG parts exhibit IR emission around 1064 nm upon excitation with a 532 nm laser, consistent with the behavior of commercially available Nd:YAG ceramics. These efforts showcase the potential for prototyping multi-scale Nd:YAG ceramic with optical gain for various applications. In the future, leveraging the high-speed printing process, μCLIP, can enable seamless adjustment in the composition and structure of the as-printed

16136829,2024, 36, Downloaded from https://onlinelibrary.wiley.com/doi/10.1002/smll.202403130 by Arizona State University Acq, Wiley Online Library on [17/10/2024]. See the Terms

on Wiley Online Library for rules of use; OA articles are governed by the applicable Creative Commons

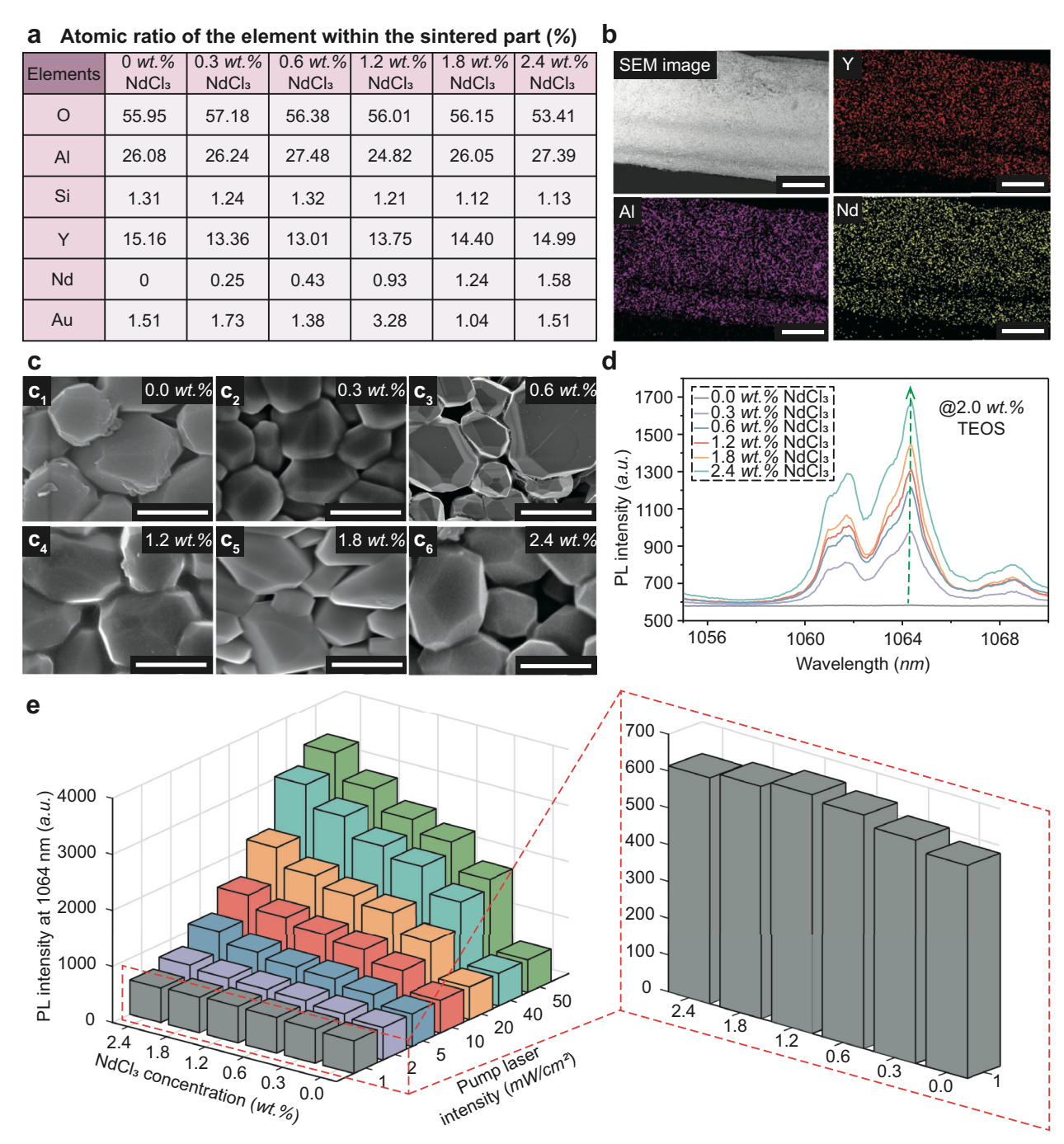


Figure 4. Characterizations of samples with varying Nd doping. (a) EDS measurements for the atomic ratio of all elements within the sintered parts. (b) SEM image and associated EDS elemental mappings of a sintered beam with a diameter of 300 μ m from resins with 2.4 wt% NdCl₃ concentration. (c) SEM images of sintered samples fabricated from resins with varying NdCl₃ concentrations. (d) PL spectra of sintered thin plates with different NdCl₃ concentrations at a constant pump laser intensity of ~10 mW cm⁻². (e) Peak intensity of PL intensities at 1064 nm of sintered thin plates under varying pump laser intensities. Scale bars: 100 μ m (b), and 4 μ m (c).

hydrogels. This capability paves the way for streamlined optimization in post-sintering processes, with the ultimate goal of improving optical characteristics, including transmission and PL performance. Furthermore, beyond its immediate utility in prototyping Nd:YAG ceramics, this approach offers valuable insights applicable to the production of diverse ceramics as lasing me-

dia, such as ruby and L_2O_3 doped Y_2O_3 , [45,72] through precise control of the photocurable resin's composition and processing conditions. Additionally, this high-speed 3D printing process also shows the potential to fabricate optical elements such as lenses and fiber couplers. Precise alignment of the pumping sources and resonators with the printed crystals enables the construction

16136829,2024, 36, Downloaded from https://onlinelibrary.wiley.com/doi/10.1002/smll.202403130 by Arizona State University Acq, Wiley Online Library on [17/10/2024]. See the Terms

) on Wiley Online Library for rules of use; OA articles are governed by the applicable Creative Commons

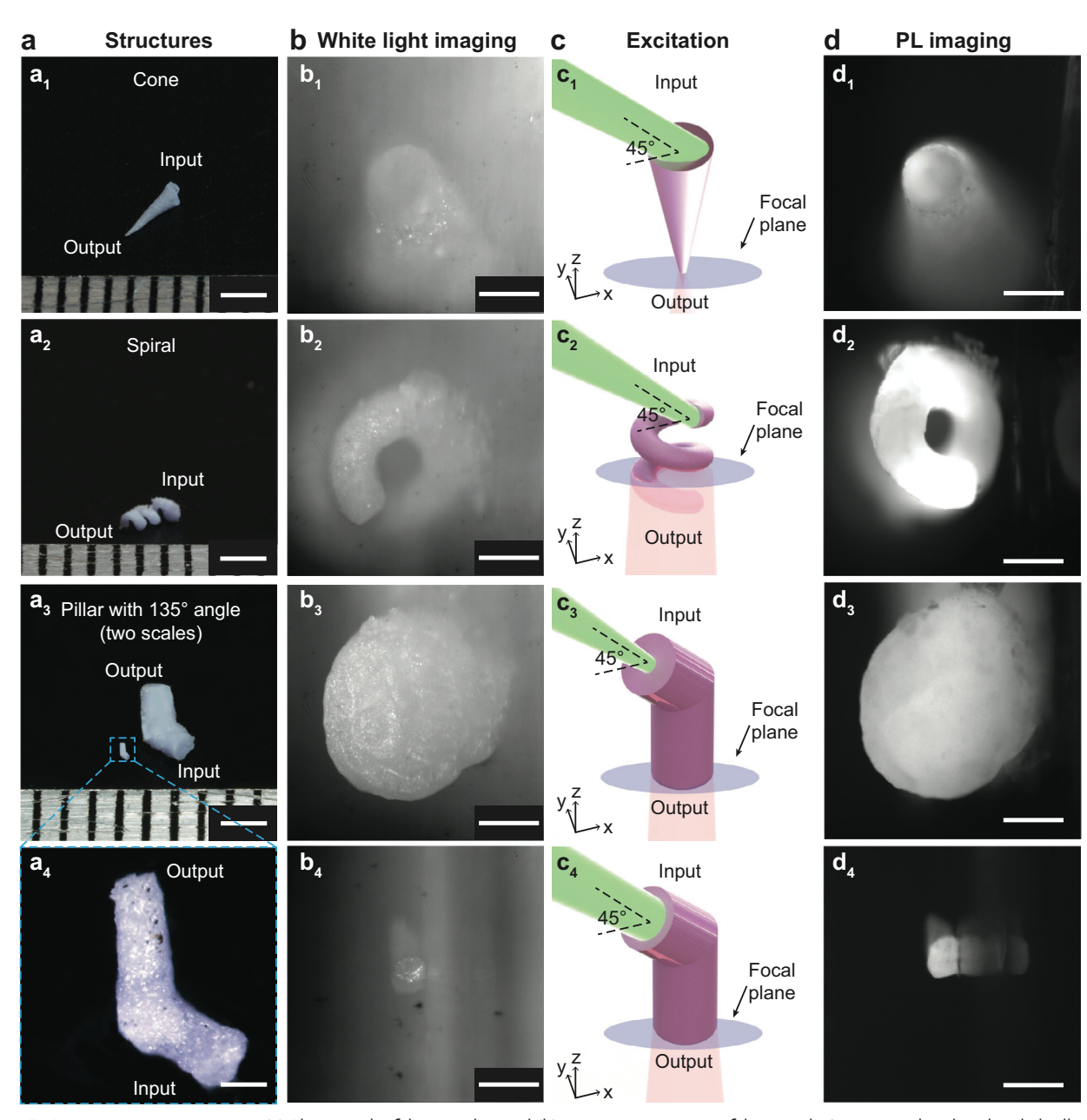


Figure 5. PL imaging measurements. (a) Photograph of the samples, and (b) microscopic images of the samples' output end under white light illumination, including cone (a_1, b_1) , spiral (a_2, b_2) , and angled pillar with different scales $(a_3, b_3, and a_4, b_4)$. (c) Schematic illustration of pumping the samples' input end with a 532 nm laser. (d) Captured PL images of the samples' output ends by filtering out the light with wavelength shorter than 594 nm. Scale bars: 2 mm (a_1-a_3) , 0.2 mm (a_4) , and 0.3 mm (b-d).

of 3D lasers with tailored geometries, providing opportunities for customized laser systems.

4. Experimental Section

Materials: Chemicals utilized in this work are all commercially available and were used as received. Yttrium chloride hexahydrate (YCl $_3$ ·6H $_2$ O, 99.9%), aluminum chloride hexahydrate (AlCl $_3$ ·6H $_2$ O, 99%), propylene oxide (PO, 99+%), ethylene glycol (99%), and deionized water (DI water, ACS) were purchased from Fisher Scientific. Neodymium chloride hexahydrate

ahydrate (NdCl $_3$ -6H $_2$ O, 99.9%), tetraethyl orthosilicate (TEOS, 99.999%), acrylic acid (AAc, 99%), and diphenyl (2,4,6-trimethylbenzoyl) phosphine oxide (TPO, 97%) were purchased from Sigma Aldrich. 1-phenylazo-2-naphthol (Sudan I, 93%) was purchased from TCI America.

Preparation of Photocurable Resins: A series of photocurable resins with different compositions were prepared for various characterizations, and their respective compositions are detailed in Table S3, S6, and S7, Supporting Information. For instance, for the resin comprising 2 wt% TEOS and 2.4 wt% $NdCl_3 \cdot 6H_2O$, the following procedure was employed: Ethylene glycol and DI water were initially weighted in a weight ratio of 2:1. The mixture was then sonicated in an ultrasonic bath for 5 minutes to

www.advancedsciencenews.com

__smal

www.small-journal.com

prepare the solvent. For 10 g printable precursor, 1.37 g YCl $_3$ ·6H $_2$ O was dissolved in 2.5 g solvent through an additional 5 minutes of sonication. Then, 1.67 g AlCl $_3$ ·6H $_2$ O, 0.24 g NdCl $_3$ ·6H $_2$ O, and 0.2 g TEOS were added to the mixture and sonicated for 30 minutes. 1.2 g AAc, 2.8 g PO, 0.01 g UV photoinitiator TPO, and 0.01 g UV absorber Sudan I, were then dissolved in the mixture through an additional 60 minutes of sonication.

Micro-Continuous Liquid Interface Printing (μCLIP): The customized μCLIP system is illustrated Figure S12, Supporting Information. The μCLIP process begins with slicing the computer-aided design (CAD) model into a series of 2D images along the printing direction (vertical axis) using a customized program with a layer thickness of 5 µm. These images are then loaded into a light engine (PRO6600, Wintech Digital) equipped with a UV light source (385 nm) and a digital micromirror device (DMD, Texas Instruments) with a resolution of $3840 \times 2160 \ pixel^2$. The patterned UV illumination is projected onto the transparent window of the resin bath with a pixel resolution of 5.8 $\mu m \times 5.8 \mu m$ at the focal plane, which is equivalent to a maximum build area of 22.27 mm × 12.53 mm. Because of the oxygen-permeable window, a thin photopolymerization-free "dead zone" exists above the window, and the fresh liquid resins can be replenished into the "dead zone" continuously during the printing. As a result, the photocurable resin can be cured into solid layers in accordance with projected images continuously. The building platform was mounted on a motorized translation stage (X-LSM200A-PTB2, Zaber Technologies Inc.), and the printing speed can be adjusted based on the speed-working curves. Additionally, a CMOS camera (MU2003-BI, AmScope) is utilized to monitor the status of the projection.

Sintering Process of As-Printed Parts: The as-printed PAAc hydrogel structures underwent a sintering process in a muffle furnace (KSL-1700X-KA, MTI). First, the as-printed structures were gradually heated up to 620 °C at a rate of 1 °C min $^{-1}$, with a 20-hour dwelling time for polymer pyrolysis. Subsequently, the samples were further heated up to 1650 °C at the same rate of 1 °C min $^{-1}$ with an additional 20-hour dwelling time for the crystallization. Finally, the furnace was cooled down to room temperature at a rate of 1 °C min $^{-1}$.

Characterization of As-printed and Sintered Parts: Optical images of both the as-printed and sintered parts were captured using a digital camera (Alpha6100, Sony) with a macro lens (FE2.8/90 MACRO G OSS, Sony). A scanning electron microscope (SEM) (Nova 200 NanoLab, FEI) with an energy-dispersive X-ray spectroscopy (EDS) detector was employed to capture SEM images of the grains and analyze the atomic ratio of elements within the sintered parts. An open-source software, Imagel, was utilized to calculate the grain sizes and porosities of sintered parts from the captured SEM images (Figure S5, Supporting Information).

Measurement of Photoluminescence Performance: Photoluminescence (PL) spectra were acquired by using a confocal Raman microscope (Alpha300 RA Ramen-AFM Microscope, WITec) equipped with a coupled spectrometer (UHTS 300 SMFC VIS, WITec) and a 532 nm diode laser with tunable light intensity (WRL-532-A-075-I-F, WITec). As illustrated in Figure S7, Supporting Information, this process involved irradiating the top surface of standard thin plate samples with a 532 nm pump laser. Subsequently, emission light from the sample was collected using a 20x objective and directed into the spectrometer.

Photoluminescence Imaging of 3D Structures: PL images were captured using a modified inverted microscope (Axio Observer D1m, Zeiss) in transmission mode. The microscope is equipped with two different light sources, a halogen light source (QTH10, Thorlabs) and a 532 nm laser (05028, LambdaPro), and a camera (Luca R EMCCD, Andor). The halogen light source was initially used to illuminate input ends of the samples, and optical images of the samples' output ends were captured using a $5\times$ objective lens (Figure $5b_1-5b_4$). Following this, a 532 nm laser beam (beam diameter: 400 µm) with a power of 1 W was directly irradiated onto the input end of the samples at a 45° incident angle with respect to the horizontal plane. The resulting PL image was collected using the same objective lens and camera, as illustrated in Figures 5c1-5c4 and S9, Supporting Information. To eliminate the influence of the pump laser, a long-pass filter with a cut-on wavelength of 594 nm (FELH0500, Thorlabs) was utilized, as shown in Figure S9, Supporting Information.

Supporting Information

Supporting Information is available from the Wiley Online Library or from the author.

Acknowledgements

This work was supported by Arizona State University (ASU) startup funding, the National Science Foundation (NSF) Future Manufacturing (FM) Award (CMMI 2229279), NSF (CMMI-1932899), NSF (CMMI-1762792), and the NSF (2227650) and Gordon and Betty Moore Foundation (41920). The authors acknowledged the use of facilities in the Eyring Materials Center at Arizona State University.

Conflict of Interest

The authors declare no conflict of interest.

Author Contributions

X.C. conceived the idea and supervised the research. L.L., W.W., S.F., S.L., and H.S. performed the experiments. All authors contributed to the data analyses and manuscript preparation and approved the submission.

Data Availability Statement

The data that support the findings of this study are available from the corresponding author upon reasonable request.

Keywords

infrared emission, micron-resolution 3D printing, neodymium-doped yttrium aluminum garnet, optical gain, photoluminescence

Received: April 18, 2024 Published online: May 15, 2024

- [1] J. E. Geusic, H. M. Marcos, L. G. Van Uitert, *Appl. Phys. Lett.* **1964**, *4*, 182.
- [2] T. H. Maiman, Nature 1960, 187, 493.
- [3] J. F. Holzrichter, Nature 1985, 316, 309.
- [4] T. Ji, T. Wang, H. Li, Q. Peng, H. Tang, S. Hu, A. Yakovlev, Y. Zhong, X. Xu, Adv. Opt. Mater. 2022, 10, 2102056.
- [5] G. Singh, Purnawirman, J. D. B. B., N. Li, E. S. Magden, M. Moresco, T. N. Adam, G. Leake, D. Coolbaugh, M. R. Watts, Opt. Lett. 2016, 41, 1189.
- [6] F. Azeem, L. S. Trainor, A. Gao, M. Isarov, D. V. Strekalov, H. G. L. Schwefel, Adv. Opt. Mater. 2022, 10, 2102137.
- [7] Y. Sato, T. Taira, Jpn. J. Appl. Phys. 2002, 41, 5999.
- [8] A. Dias-Santos, J. Ferreira, L. Abegão Pinto, I. Domingues, J. P. Silva, J. P. Cunha, M. Reina, Int Ophthalmol 2015, 35, 173.
- [9] D. C. Saunders, Brit. J. Ophthalmol. 1990, 74, 523.
- [10] R. Valcavi, F. Riganti, A. Bertani, D. Formisano, C. M. Pacella, *Thyroid* 2010, 20, 1253.
- [11] F. Sun, X. Sun, Q. Shi, Y. Zhai, Medicine 2018, 97, 13360.
- [12] J. A. Ledon, J. Savas, K. Franca, A. Chacon, K. Nouri, *Lasers Med Sci* 2014, 29, 823.

www.small-journal.com

16136829, 2024, 36, Downloaded from https://onlinelibrary.wiley.com/doi/10.1002/sml1020403130 by Arizona State University Acq. Wiley Online Library on [17/10/2024]. See the Terms and Conditions (https://onlinelibrary.wiley

on Wiley Online Library for rules of use; OA articles are governed by the applicable Creative

- [13] F. Rezazadeh, P. Dehghanian, D. Jafarpour, J Lasers Med Sci 2018, 10, 1.
- [14] M. Roncati, A. Gariffo, Photomedicine and Laser Surgery 2014, 32, 186.
- [15] V. G. A. Suter, S. Sjölund, M. M. Bornstein, Lasers Med Sci 2017, 32,
- [16] P. De Coster, S. Rajasekharan, L. Martens, Int J Paediatr Dent 2012.
- [17] K. Gurusami, D. Chandramohan, S. Dinesh Kumar, M. Dhanashekar, T. Sathish, Materials Today: Proceedings 2020, 21, 981.
- [18] B. R. Moharana, S. K. Sahu, A. Maiti, S. K. Sahoo, T. K. Moharana, Materials Today: Proceedings 2020, 33, 5262.
- [19] C. Leone, S. Genna, Composites, Part B 2018, 140, 174.
- [20] A. Maity, S. Maithani, M. Pradhan, Anal. Chem. 2021, 93, 388.
- [21] Y. Hibino, F. Hanawa, H. Nakagome, M. Ishii, N. Takato, J. Lightwave Technol. 1995, 13, 1728.
- [22] N. Pavel, M. Tsunekane, T. Taira, Opt. Express 2011, 19, 9378.
- [23] S.-H. Lee, S. Kochawattana, G. L. Messing, J. Q. Dumm, G. Quarles, V. Castillo, J American Ceramic Society 2006, 89, 1945.
- [24] R. Boulesteix, A. Maître, J.-F. Baumard, C. Sallé, Y. Rabinovitch, Optical Materials 2009, 31, 711.
- [25] Y. Li, S. Zhou, H. Lin, X. Hou, W. Li, H. Teng, T. Jia, J. Alloys Compd. 2010, 502, 225.
- [26] J. Li, Y. Wu, Y. Pan, W. Liu, L. Huang, J. Guo, Int. J. Appl. Ceram. Technol. 2008, 5, 360.
- [27] L. Ge, J. Li, Z. Zhou, B. Liu, T. Xie, J. Liu, H. Kou, Y. Shi, Y. Pan, J. Guo, Optical Materials 2015, 50, 25.
- [28] F. Kotz, K. Arnold, W. Bauer, D. Schild, N. Keller, K. Sachsenheimer, T. M. Nargang, C. Richter, D. Helmer, B. E. Rapp, Nature 2017, 544, 337.
- [29] J. Bauer, C. Crook, T. Baldacchini, Science 2023, 380, 960.
- [30] G. Zhang, D. Carloni, Y. Wu, Ceram. Int. 2020, 46, 17130.
- [31] G. A. Dosovitskiy, P. V. Karpyuk, P. V. Evdokimov, D. E. Kuznetsova, V. A. Mechinsky, A. E. Borisevich, A. A. Fedorov, V. I. Putlayev, A. E. Dosovitskiy, M. V. Korjik, CrystEngComm 2017, 19, 4260.
- [32] J. Winczewski, M. Herrera, C. Cabriel, I. Izeddin, S. Gabel, B. Merle, A. Susarrey Arce, H. Gardeniers, Adv. Opt. Mater. 2022, 10, 2102758.
- [33] H. Wang, L. Y. Liu, P. Ye, Z. Huang, A. Y. R. Ng, Z. Du, Z. Dong, D. Tang, C. L. Gan, Adv. Mater. 2021, 33, 2007072.
- [34] F. Kotz, P. Risch, K. Arnold, S. Sevim, J. Puigmartí-Luis, A. Quick, M. Thiel, A. Hrynevich, P. D. Dalton, D. Helmer, B. E. Rapp, Nat. Commun. 2019. 10. 1439.
- [35] J. Yang, M. Feng, K. Zhang, Z. Chen, R. Xu, A. Khan, Y. Li, J. Xie, L. Liu, F. Song, W. Huang, Adv. Opt. Mater. 2022, 10, 2201110.
- [36] Z. Seeley, T. Yee, N. Cherepy, A. Drobshoff, O. Herrera, R. Ryerson, S. A. Payne, Optical Materials 2020, 107, 110121.
- [37] I. K. Jones, Z. M. Seeley, N. J. Cherepy, E. B. Duoss, S. A. Payne, Optical Materials 2018, 75, 19.
- [38] G. Zhang, Y. Wu, Addit. Manuf. 2021, 47, 102271.
- [39] S. Liu, W. Wang, W. Xu, L. Liu, W. Zhang, K. Song, X. Chen, Research **2022**, 2022, 9790307.
- [40] M. Z. Rong, M. Q. Zhang, W. H. Ruan, Mater. Sci. Technol. 2006, 22,
- [41] L. M. Hamming, R. Qiao, P. B. Messersmith, L. C. Brinson, Compos. Sci. Technol. 2009, 69, 1880.

- [42] M. Vozárová, E. Neubauer, Ľ. Bača, M. Kitzmantel, J. Feranc, V. Trembošová, P. Peciar, M. Kritikos, M. Orlovská, M. Janek, M. Matejdes, J. Eur. Ceram. Soc. 2023, 43, 1751.
- [43] J. Liu, A. Lal, R. M. German, Acta Mater. 1999, 47, 4615.
- [44] A. Krell, J. Klimke, J American Ceramic Society 2006, 89, 1985.
- [45] I. Cooperstein, S. R. K. C. Indukuri, A. Bouketov, U. Levy, S. Magdassi, Adv. Mater. 2020, 32, 2001675.
- [46] X. Qin, G. Zhou, Y. Yang, J. Zhang, X. Shu, S. Shimai, S. Wang, Ceram. Int. 2014, 40, 12745.
- [47] H. Gao, H. Li, G. F. R. Chen, P. Xing, M. C. Tan, D. T. H. Tan, Sci. Rep. 2021, 11, 21292.
- [48] F. Kotz, A. S. Quick, P. Risch, T. Martin, T. Hoose, M. Thiel, D. Helmer, B. E. Rapp, Adv. Mater. 2021, 33, 2006341.
- [49] J. Yang, T.-U. Yin, W.-M. Xu, L.-G. Xia, A.-B. Li, J. Hu, Photomedicine and Laser Surgery 2006, 24, 625.
- [50] W. Wang, S. Liu, L. Liu, S. Alfarhan, K. Jin, X. Chen, ACS Materials Lett **2023**, *5*, 1727.
- [51] X. Guo, W. Li, K. Nakanishi, K. Kanamori, Y. Zhu, H. Yang, J. Eur. Ceram. Soc. 2013, 33, 1967.
- [52] J. R. Tumbleston, D. Shirvanyants, N. Ermoshkin, R. Janusziewicz, A. R. Johnson, D. Kelly, K. Chen, R. Pinschmidt, J. P. Rolland, A. Ermoshkin, E. T. Samulski, J. M. DeSimone, Science 2015, 347, 1349.
- [53] H. O. T. Ware, C. Sun, Journal of Micro and Nano-Manufacturing 2019, 7, 031001.
- [54] G. Shao, R. Hai, C. Sun, Adv. Optical Mater. 2020, 8, 1901646.
- [55] L. Liu, S. Liu, M. Schelp, X. Chen, ACS Appl. Mater. Interfaces 2021, 13. 29122
- [56] X. Chen, W. Liu, B. Dong, J. Lee, H. O. T. Ware, H. F. Zhang, C. Sun, Adv. Mater. 2018, 30, 1705683.
- [57] O. Wichterle, D. Lím, Nature 1960, 185, 117.
- [58] J.-Y. Sun, X. Zhao, W. R. K. Illeperuma, O. Chaudhuri, K. H. Oh, D. J. Mooney, J. J. Vlassak, Z. Suo, Nature 2012, 489, 133.
- [59] T. Zhou, H. Yuk, F. Hu, J. Wu, F. Tian, H. Roh, Z. Shen, G. Gu, J. Xu, B. Lu, X. Zhao, Nat. Mater. 2023, 22, 895.
- [60] D. Kouznetsov, J.-F. Bisson, K. Takaichi, K. Ueda, J. Opt. Soc. Am. B 2005. 22. 1605.
- [61] M. Stuer, P. Bowen, M. Cantoni, C. Pecharroman, Z. Zhao, Adv. Funct. Mater. 2012, 22, 2303.
- [62] A. Wagner, Y. Meshorer, B. Ratzker, D. Sinefeld, S. Kalabukhov, S. Goldring, E. Galun, N. Frage, Sci. Rep. 2021, 11, 1512.
- [63] A. Maître, C. Sallé, R. Boulesteix, J.-F. Baumard, Y. Rabinovitch, J. American Ceramic Society 2008, 91, 406.
- [64] M. Zhou, B. Tang, S. Zhang, Ceram. Int. 2021, 47, 12826.
- [65] A. Ikesue, K. Kamata, K. Yoshida, J. Am. Ceram. Soc. 1996, 79, 1921.
- [66] F. Wang, B. Yang, X. Chen, W. Ma, B. Xu, Mater. Chem. Phys. 2016, 169, 113,
- [67] G. Ju, Y. Hu, L. Chen, X. Wang, Z. Mu, Phys. B 2013, 415, 1.
- [68] H. F. Brito, J. Hölsä, T. Laamanen, M. Lastusaari, M. Malkamäki, L. C. V. Rodrigues, Opt. Mater. Express 2012, 2, 371.
- [69] Y. Li, Y. Wang, Y. Gong, X. Xu, F. Zhang, Acta Mater. 2011, 59, 3174.
- [70] Q. Liu, J. Liu, J. Li, M. Ivanov, A. Medvedev, Y. Zeng, G. Jin, X. Ba, W. Liu, B. Jiang, Y. Pan, J. Guo, J. Alloys Compd. 2014, 616, 81.
- [71] H. Gao, J. An, C. K. Chua, D. Bourell, C.-N. Kuo, D. T. H. Tan, Mater. Today 2023, 69, 107.
- [72] W. H. Rhodes, J American Ceramic Society 1981, 64, 13.